Electrochimica Acta 574 (2026) 149354

Contents lists available at ScienceDirect

Electrochimica Acta

journal homepage: www.journals.elsevier.com/electrochimica-acta

In situ ec-AFM investigation of a high-capacity aluminum-organic battery: Visualizing anion-induced swelling in redox-active polymer electrodes

Sven Daboss [a,b,*], Eva Bräutigam [c], Birgit Esser [b,c], Tobias Cramer [d], Mete Batuhan Durukan [e,f], Simon Fleischmann [b,e,f], Christine Kranz [a,b,*]

[a] Ulm University, Institute of Analytical and Bioanalytical Chemistry, Albert-Einstein-Allee 11, Ulm, 89081, Germany
[b] Ulm University, CELEST Green Energy Lab Ulm, Lise-Meitner-Str. 16, Ulm, 89081, Germany
[c] Ulm University, Institute of Organic Chemistry II and Advanced Materials, Albert-Einstein-Allee 11, Ulm, 89081, Germany
[d] University of Bologna, Department of Physics and Astronomy, Viale Berti Pichat 6/2, Bologna, 40127, Italy
[e] Helmholtz Institute Ulm, Helmholtzstr. 11, Ulm, 89081, Germany
[f] Karlsruhe Institute of Technology, Karlsruhe, 76021, Germany

ARTICLE INFO

Keywords:
ec-AFM
Aluminum-based batteries
Redox-active polymer electrodes
Post-lithium energy storage
Electrode swelling

ABSTRACT

Rechargeable aluminum batteries (RABs) are promising post-lithium energy storage systems due to the high abundance and volumetric capacity of aluminum, yet stable positive electrodes development remains a bottleneck. Cross-linked poly(3-vinyl-N-methylphenothiazine) (X-PVMPT) as a p-type redox polymer shows reversible two-electron redox chemistry at relatively high potentials and excellent cycling stability in RABs when paired with chloroaluminate-based ionic liquid electrolytes. Here, we present the investigation of volume expansion and morphological evolution of X-PVMPT composite electrodes during cycling using electrochemical (ec-) atomic force microscopy (AFM) and cyclic voltammetry. ec-AFM data reveals the dynamics of reversible expansion during anion insertion and (ir)reversible changes associated with prolonged cycling. In situ linescan profiling and 2D nanomechanical imaging allows visualization of pronounced and reversible volume change during cycling, associated with the insertion of $AlCl_4^-$/ $Al_2Cl_7^-$ anions. Complementary electrochemical quartz crystal microbalance with dissipation monitoring (EQCM-D) measurements validate these observations at the macroscopic scale, confirming that volume expansion and electrochemical stiffening are homogeneous, bulk phenomena of the X-PVMPT framework. We determined a reversible swelling amplitude of 1.1 ± 0.1 μm during anion insertion for a 9.6 μm thick film, correlated with a 4-fold increase in stiffness. While initial cycles involve large-scale structural changes, the network rapidly reaches a mechanically stabilized state after the initial cycle, where the polymer matrix undergoes irreversible reorganization. After the steady-state phase (from cycle 120 onwards), the swelling amplitude drops by 60–75% to 0.3 – 0.4 μm with sustained faradaic performance, highlighting the ability of the cross-linked matrix to establish ion-conduction pathways during prolonged cycling.

1. Introduction

The required transition to electrification in transportation, consumer electronics, and stationary energy storage will be based on efficient, sustainable, and cost-effective battery technologies. Rechargeable aluminum batteries (RABs) have emerged as an attractive class of post-lithium electrochemical energy-storage systems due to earth-abundant and inexpensive resources and aluminum's potential for high volumetric capacity (8040 mA h cm^{-3}), surpassing that of lithium (2046 mA h cm^{-3}) [1]. Despite these advantages, the RAB technology is still considered in its infancy due to several intrinsic challenges, most notably, the scarcity of efficient and stable positive electrode materials that can reversibly accommodate Al-based charge carriers [2,3].

Organic active materials (OAMs) have emerged as promising cathode materials for post-lithium cells due to their tunable redox potentials, their low-density, structural versatility, low toxicity and potential sustainability aspects if obtained from renewable raw materials [4–7]. OAMs allow for a broad spectrum of reversible redox reactions enabling a variety of charge (and concurrent ion) storage pathways [8,9]. n-type materials undergo reductive transitions to accommodate cations, while p-type materials undergo oxidative transitions to bind electrolyte anions. Bipolar organics can combine both mechanisms depending on the

* Corresponding authors.
E-mail addresses: sven.daboss@uni-ulm.de (S. Daboss), christine.kranz@uni-ulm.de (C. Kranz).

https://doi.org/10.1016/j.electacta.2026.149354
Received 30 April 2026; Received in revised form 10 June 2026; Accepted 15 June 2026
Available online 17 June 2026

cell configuration [10]. As a result, p-type OAMs represent a fundamentally different approach to charge storage compared to traditional metal oxides in conventional metal-ion batteries by facilitating anion uptake rather than cation intercalation. At the same time, they exhibit strong compatibility with multivalent metal ions [11,12]. Unlike traditional inorganic intercalation electrodes, which often suffer from sluggish kinetics due to the high charge density of multivalent cations causing strong electrostatic interactions within the rigid host lattice, OAMs feature a more flexible framework [13]. Specifically, p-type OAMs bypass the 'cation-sluggishness' entirely by utilizing an anionic charge-storage mechanism. They can be effectively utilized in anionic cell configurations, where charge compensation is achieved through the rapid surface-near incorporation of bulky anions like $AlCl_4^-$/$Al_2Cl_7^-$ [14]. This mechanistical shift from cation to anion coordination significantly reduces the activation energy for ion transport, potentially enabling high-power density applications in RABs. Despite this excellent performance parameter, organic electrodes still face challenges, notably solubility/dissolution [15] in the electrolyte and limited electronic conductivity [16] that requires composite materials that may lead to incomplete suppression of parasitic side reactions especially in reactive chloroaluminate electrolytes [17].

Phenothiazine (PT)-based polymers such as poly(3-vinyl-N-methylphenothiazine) (PVMPT) and its cross-linked derivative (X-PVMPT) display high redox potentials (e.g., PT can undergo two reversible oxidations to a dication at potentials of 3.6 and 4.1 V vs. Li/Li^+) and excellent rate/cycling performance up to 5000 cycles at a 10C rate (88% capacity retention) for a RAB [6]. The cross-linking suppresses dissolution and enables access to higher reversible capacities [18–21]. X-PVMPT has shown excellent performance as a positive electrode material in RABs in 1-ethyl-3-methylimidazolium (EMIm)-chloroaluminate electrolyte. The cell showed reversible two-electron redox behavior and high practical specific capacities (up to 167 $mA{\cdot}h{\cdot}g^{-1}$) together with excellent rate capability and long cycle life (hundreds of cycles under optimized conditions) [6,19]. However, the high capacity and fast kinetics of X-PVMPT rely on the reversible accommodation of bulky anions, a process that gives rise to chemo-mechanical strain within the cross-linked matrix. Electrochemically induced ion insertion underpins charge storage in secondary batteries and pseudocapacitors [22,23]. During cycling, ion insertion and adsorption are accompanied by electron transfer, leading to electrode deformations originating from localized distortions and pore volume changes on the macroscopic scale. Developing high-performance RABs requires a systematic evaluation of the dependence between this anion uptake, the resulting mechanical strain and the dimensional stability of the electrode host.

A critical issue for aluminum-based, rechargeable batteries is electrode swelling related to the insertion of large anions such as $AlCl_4^-$ / $Al_2Cl_7^-$ [24]. Swelling can arise from reversible or irreversible volume changes during ion insertion/extraction leading to mechanical expansion/contraction, parasitic side reactions at the current collectors or electrode/electrolyte interfaces contributing to capacity fade. In RABs, this issue is particularly pronounced, as the incorporation of large chloroaluminate anions (e.g. $AlCl_4$) causes rapid electrode swelling, which further weakens interfacial adhesion and may lead to the detachment of electrode materials from the current collector [25,26]. The relationship between electrode deformation and stored charge strongly depends on the specific battery material [27] and has been reported in the literature for Li-ion batteries (LIBs). For example, in situ dilatometry was used to quantify the reversible intercalation-induced and irreversible passivation-induced solid electrolyte interphase (SEI) formation thickness changes in graphite anodes and lithium nickel manganese cobalt oxides (NMC) cathodes [28]. Li-ion intercalation in graphite varies from linear behavior [27,29] to more complex dependencies involving higher-order derivatives of deformation with respect to charge [30]. To evaluate these complex phenomena related to swelling of the electrode material, in situ measurement techniques including multi-beam optical stress sensors (MOSS), digital image correlation (DIC), and bending-curvature measurement systems (BCMS) have been employed [31]. Studies on conductive polymers such as polypyrrole (PPy), have provided fundamental insights into the mechanical response of organic networks, demonstrating that strain evolution is directly linked to the size and hydration shell of ions moving in and out of the polymer matrix [32–34]. By employing in situ curvature measurements [35], real-time stress evolvement and interfacial fracture energy were investigated for PPy active materials. While traditional methods, like electrochemical quartz crystal microbalance (EQCM), effectively track mass changes during ion flux, recent literature has shifted towards advanced imaging to capture changes in the electrode's structural parameters, such as modulus evolution and localized distortions to directly visualize local mechanical deformation. Recently, operando substrate curvature measurements were utilized to distinguish between electrochemical and mechanical contributions to stress evolution and particle rearrangement in lithium iron phosphate (LFP) composite electrodes [36] and in hard carbon composite electrodes, which revealed a significant asymmetry in expansion between the sodiation and desodiation pathways [37].

Scanning probe microscopy (SPM) techniques [38] and in particular atomic force microscopy (AFM) and related techniques provide high-resolution information on surface morphology and nanomechanical properties such as stiffness, adhesion, and deformation - under operating conditions [39,40]. For example, electrochemical AFM (ec-AFM) has been used to visualize the formation and growth of the SEI on graphite anodes, providing spatial resolution far exceeding traditional dilatometry [37]. Early in situ ec-AFM studies focused on amorphous Sn-Co-C films during electrochemical cycling vs. Li-metal in 1 M $LiPF_6$ in carbonate-based electrolyte [41]. By tracking the height changes a reversible volume expansion occurring without fracture or mechanical failure was observed demonstrating that the expansion is a linear function of lithium content and is significantly reduced by the incorporation of carbon and cobalt. Electrochemical strain microscopy (ESM) [42] and modulated electrochemical (mec)-AFM [43] have been applied to characterize interfaces and to map surface changes by detecting local electrochemical strain induced by ion redistribution and charge-density modulation. mec-AFM was also used to probe depth-dependent ion migration and electroswelling in PPy:DBS actuators [44], and to map local electroactuation and charge uptake in organic mixed ionic-electronic conductors (OMIECs) [45]. Wang et al. utilized operando AFM dilatometry on tungsten oxide to show that structural water enables a transition from battery to pseudocapacitive behavior by facilitating a smaller mechanical response compared to the large, irreversible distortions seen in anhydrous WO_3 [46]. Recently, mechanical cyclic voltammetry (mCV), a combination of in situ ec-AFM and cycling the potential, was used to track time-resolved deformation during electrochemical cycling. mCV links local mechanical responses to electrochemical activity, providing nanoscale insight into charge storage dynamics [27,46,47].

Herein, we present in situ ec-AFM to investigate the dynamic structural and mechanical changes during ion insertion and extraction in redox-active crosslinked X-PVMPT polymeric composite electrodes in $AlCl_3$/[EMIm]Cl electrolyte by utilizing in situ height profiling and nanomechanical imaging. By directly correlating electrochemical activity with local structural and mechanical responses, this approach identifies structural reversibility and volume expansion, focusing on the different stages of the active material.

To the best of our knowledge, the volume expansion and contraction of X-PVMPT in battery electrodes have not been investigated, neither in RABs nor in LIBs.

2. Experimental section

2.1. Electrolyte and electrodepreparation

The electrolyte was prepared by mixing dried aluminum chloride

($AlCl_3$, 99.999%, Sigma-Aldrich, Germany) and 1-ethyl-3-methylimidazolium chloride ([EMIm]Cl > 98%, Iolitec, Germany) in a molar ratio of 1.5:1 under inert argon atmosphere inside a glovebox (Unilab, MBraun, Germany) with oxygen and water levels below 0.1 ppm, until a homogeneous ionic liquid was obtained. For a comparative study in the absence of $AlCl_4$ ions a mixture of [EMIm]Cl and ethylene glycol (EG, 98%, Acros Organics) in a ratio of 1:2 [48] was prepared by mixing the two components at room temperature and stirred continuously for 2 h to obtain a homogeneous solution.

Due to the geometrical constraints of the AFM electrochemical cell, an embedded microelectrode, fitting the geometric requirements of the AFM electrochemical cell, was prepared. A segment of a gold microwire (d = 25 μm, length = 1 cm, 99.9%, Goodfellow, United Kingdom) was embedded in epoxy resin and polished to expose the Au surface on both sides of the resin block. Embedding was performed with a two-component epoxy resin (EpoFix, Struers GmbH, Germany) employing a two-step vacuum procedure, followed by curing for 12 h. The cured epoxy blocks were subsequently polished using SiC abrasive paper and diamond lapping films (6 μm, 3 μm and 1 μm; Leco Corporation, USA). The polishing quality was assessed using optical microscopy (VHX-7000, Keyence, Japan). Electrical contact was then established on the backside using silver paste and a stainless-steel disc connected to a copper wire.

The crosslinked X-PVMPT polymer [6] with 10 mol% of the crosslinker was synthesized as reported elsewhere[49]. Composite electrodes were fabricated by combining 50 wt% X-PVMPT, 45 wt% carbon black (acetylene black, 99.9+%, Alfa Aesar, Germany), and 5 wt% poly (vinylidene difluoride) (PVdF, Kynar HSV 900, Arkema, France). The components were mixed and dispersed in N-methyl-2-pyrrolidone (NMP, 99.5%, Thermo Scientific, Germany, stored over molecular sieves) using a planetary centrifugal mixer (ARM 310, Thinky Mixer, Japan). The resulting slurry was drop-casted onto the prepared embedded microelectrode (approximately d = 50 μm using optical microscopy (Figure S1). The coated microelectrode was dried at 60 °C for 12 h under ambient pressure, followed by vacuum drying for 2 h. To determine the electrode thickness, a cross-section was prepared using focused ion beam (FIB) microscope and subsequently imaged via scanning electron microscopy (SEM).

2.2. Electrochemical experiments

All measurements were conducted inside a glovebox. Electrochemical cycling was performed in an electrolyte with $AlCl_3$/[EMIm]Cl in a ratio of 1.5:1 as electrolyte with the embedded X-PVMPT-modified microelectrode as the working electrode and an Al wire as reference/counter electrode, connected to a (bi)potentiostat (CHI760E, CHInstruments, USA). Cyclic voltammetry (CV) was performed at a scan rate of 5–10 mV/s in a potential range of 0.3–2.2 V vs. Al/Al^{3+}. AC—CV was implemented using a lockin-amplifier (MFLI, Zurich Instruments, Switzerland) at a scan rate of 2 mV/s using an oscillation frequency of 37 Hz or 77 Hz with an amplitude of 100 mV. EIS measurements were carried out using a battery cycler (MPG200, BioLogic, France) at room temperature after a 24 h resting phase at open-circuit voltage (OCV). These measurements were performed in a three-electrode configuration using a Swagelok-type cell, equipped with the X-PVMPT composite working electrode and aluminum as counter and reference electrodes. The EIS spectra were recorded at a potential of 1.6 V vs. Al/Al^{3+} across a frequency range from 100 kHz down to 10 mHz using a sinusoidal voltage amplitude of 10 mV under potentiostatic control after 1, 10 and 150 cycles.

2.3. AFM and forcespectroscopy

AFM measurements were performed using a Park NX10 (Park Systems, South Korea) located in the glovebox. Silicon probes (RTESPAW–150, Bruker, Germany) with a nominal spring constant of k = 6.0 N/m and a resonance frequency of 150 kHz at a scan speed of 0.1–1.0 Hz were used. Prior to measurements, the force constants of the cantilevers were determined using the thermal noise method [50].

Nanomechanical linescan maps were obtained at a sweep rate of 10.0–20.0 μm/s with loading forces of 50 nN (10.0 μm with 128 pixels in x-direction and 1024 pixel in y-direction) using ParkSystems PinPoint™mode. Nanomechanical PinPoint maps (10.0 × 10.0 μm, 128 × 128) were obtained using a sweep rate of 10.0 μm/s with loading forces of 50 nN. Data analysis was carried out using MountainSPIP (version 9.3.10663, Digital Surf, France), XEI (version 5.2.0, ParkSystems, South Korea) and OriginPro (version 2019b, OriginLab Corporation, USA).

To extract the roughness parameter, S_a and S_z, AFM measurements were performed in nanomechanical mode (five 3.0 × 3.0 μm areas) (see Figure S2). Cross-sectional line profiles were extracted from the AFM height maps in the spatiotemporal obtained maps to determine the R_a and R_z values. This evaluation was performed by selecting three distinct locations on each sample, with each measurement consisting of 10 averaged linescans to ensure statistical reliability and minimize local noise. The mec-AFM measurements were conducted using an external MFLI lock-in amplifier (Zurich Instruments, Switzerland). A generated sine wave with a controlled amplitude and offset voltage was applied to the working electrode as the output signal, while the amplified PSPD signal from the AFM served as the input.

For a direct comparison of the electrode surface before and after extended electrochemical cycling, AFM topography images were additionally recorded in dynamic mode using silicon cantilevers (RTESPAW-150, Bruker, Germany) at a scan area of 10 × 10 μm and a scan rate of 0.2–0.4 Hz. Both the pristine and the cycled electrodes (150 cycles) were characterized in ambient conditions (glovebox). To remove the bulk electrolyte prior to the AFM imaging, the cycled electrode was gently rinsed with 1,2-difluorobenzene (TCI Chemicals, Germany).

2.4. FIB/SEM

SEM imaging and energy dispersive X-ray spectroscopy (EDX) were performed with an Apreo 2s and a Quanta FEG 3D system (ThermoFisher Scientific, USA).SEM images were obtained at 5 kV, 86 pA and EDX measurements using a primary electron beam at 5 kV, 1.6 nA. Imaging processing was carried out using Fiji (version 2.14.0**)** [51]. Before cross-sectioning the composite electrode using a dual beam system (Quanta FEG 3D,ThermoFisher Scientific, USA), a thin Pt layer was sputtered onto the sample to reduce charging effects (approximately 10 nm). A platinum layer of approx. 300 nm was deposited using ion beam-induced deposition (IBID) with methylcyclopentadienyl trimethyl platinum ($C_9H_{16}Pt$) as precursor.

2.5. EQCM-D measurements

EQCM measurements with dissipation monitoring (EQCM-D) measurements were performed using an AWS X1 instrument (AWSensors, Spain) equipped with a temperature control unit, connected with a potentiostat (SP-300, Bio-Logic, France). The scan rate was set to 10 mV/s for 5 cycles within a potential window of 0.3 - 2.2 V vs. Al/Al^{3+}. An air-tight two-electrode cell was utilized, employing a gold-coated AT cut quartz crystal resonator (fundamental frequency of 5 MHz) as WE, an Al-wire as combined RE/CE, and the aforementioned electrolyte (1 mL). The cell temperature was maintained at 23 °C throughout the measurements.

The WE was prepared by spraying the composite slurry diluted with NMP (c = 1 mg mL^{-1}) onto the gold surface of the resonator that was kept at 120 °C on a hot plate. Then, the electrodes were subjected to vacuum drying at 60 °C for 2 h to ensure the complete removal of residual solvent. The active material loading was determined to be approximately 50 μg (47 μg cm^{-2}) derived from the frequency shift before and after the coating of the resonator. All assembly steps were conducted in a glovebox environment to prevent contamination of the

moisture-sensitive chloroaluminate electrolyte.

3. Results and discussion

3.1. ec-AFM setupand electrochemicalcharacterization

To examine the structural and mechanical properties underpinning electrochemical performance in RABs, we investigated the swelling behavior of the redox-active X-PVMPT polymer cathode against an aluminum anode during cycling using ec-AFM. Based on previous electrochemical studies of X-PVMPT [6], which revealed a high-capacity two-electron redox process (up to 167 $mA{\cdot}h{\cdot}g^{-1}$) and excellent cycling stability in chloroaluminate electrolyte, our approach allows for the real-time visualization of nanoscale morphological changes associated with $AlCl_4^-$ and $Al_2Cl_7^-$ ion insertion and extraction. Because conventional wire-in-glass microelectrodes are incompatible with the AFM cell geometry, the measurements were obtained using a custom epoxy-embedded gold microelectrode as detailed in the Experimental Section and depicted in Fig. 1. The use of modified microelectrodes offers several advantages for the conducted studies in comparison to conventional coin-cell electrodes, which are related to reduced ohmic and mass-transport limitations and enhanced sensitivity to local electro-chemo-mechanical responses. This configuration enables the intrinsic behavior of the active material to be probed under well-defined electrochemical conditions.

Fig. 1a shows the schematic setup of the ec-AFM configuration, the stepwise redox processes of X-PVMPT (Fig. 1b), and cyclic voltammograms (CVs) recorded at the embedded microelectrodes. The CVs exhibit well-defined and increasingly stable anodic and cathodic peaks over the first ten cycles in agreement with the literature, demonstrating quasi-reversible charge transfer and the electrochemical stability of the polymeric composite electrode.

Fig. 1a depicts the experimental setup with the X-PVMPT-modified microelectrode as working electrode versus an Al RE/CE. The SEM and AFM images (Fig. 1a, insets) confirm the presence of the polymeric coating on the microelectrode surface and provide an overview of the resulting surface topography. While previous studies of X-PVMPT reported only on mass loading [6], we used FIB/SEM cross-sectional analysis (Figure S3), to determine also the average thickness value of 9.6 ± 0.2 µm. As shown in Fig. 1b, the redox activity of X-PVMPT involves the formation of ion-paired species, where the polymer matrix stabilizes incoming Al-based anions upon charging [6]. This two-electron redox process is shown in the CVs (Fig. 1c), revealing quasi-reversible redox behavior consistent with the two sequential one-electron oxidations (e.g., 0.85 V vs. Al/Al^{3+} in cycle 1) to the radical and di-cationic state (1.67 V and 2.02 V vs. Al/Al^{3+}). In the cathodic scan direction, the peak potential for the second redox event is observed at 1.43 V vs. Al/Al^{3+}. The stability of these profiles at a scan rate of 10 mV/s demonstrates not only the electrochemical robustness of the polymer film, but also its ability to facilitate rapid ion diffusion, a prerequisite for the dynamic mechanical analysis performed in the following studies.

3.2. In situ investigation of the polymer swelling

The real-time nanomechanical response of the X-PVMPT composite electrode during cycling was investigated using in situ contact-mode ec-AFM, as shown in Figure S4. Please note, for recording these images the y-axis of the AFM scanner was disabled and therefore the images represent repetitive x-linescans that are stacked along the y-axis to construct a spatiotemporal map. Consequently, the y-axis simultaneously represents both the progression of time and changes related to the applied potential. The potential drift from the left to the right side of each individual scan line is approximately 1 mV due to the used scan

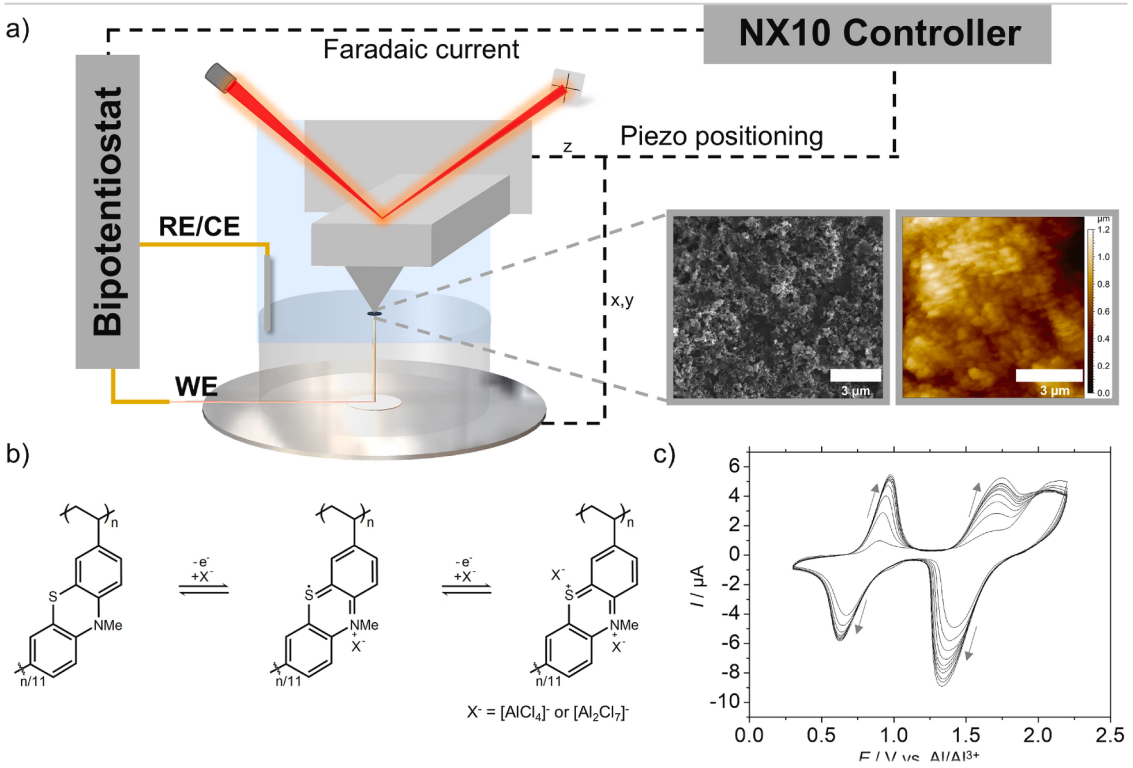

Fig. 1. a) Schematic illustration of the ec–AFM setup. Faradaic currents generated at the electrode surface are measured during simultaneous contact-mode AFM imaging, nanomechanical linescans or maps. Representative SEM (left) and AFM (right) images showing the electrode surface morphology of the pristine, composite X-PVMPT-modified microelectrode. b) Redox chemistry of X-PVMPT, depicting sequential oxidation steps and formation of ion-paired species with Al-based anions. c) Cyclic voltammetry showing the first 10 cycles recorded vs. Al/Al^{3+} demonstrating the quasi-reversible redox behavior and electrochemical stability of the polymer film at a scan rate of 10 mV/s.

velocity of 1 Hz, ensuring that each line represents a nearly isopotential state. Time-space height maps acquired during cycling (Figure S4a) reveal a distinct and periodic modulation of the polymer surface that is tightly synchronized with the applied potential. The topographical imaging reveals pronounced but reversible surface expansion correlated with the redox states of the phenothiazine units. Upon anodic polarization at a potential of 1.80 V, corresponding to the oxidation of X-PVMPT and anion ($AlCl_4^-$) insertion, the electrode surface exhibits a gradual increase in height and roughness ($R_a = 24.8 \pm 1.2$ nm in the reduced state vs. 55.1 ± 2.3 nm in the oxidized state, with R_z increasing from 123.6 ± 7.2 nm to 235.5 ± 33.5 nm, respectively), indicative of the polymer network swelling. During the cathodic scan, the polymer is reduced, associated with the relaxation of the swollen structure at 1.5 V vs. Al/Al^{3+}, suggesting the release of charge-compensating anions from the polymer matrix. The observed contrast evolution in the height image (Figure S4a) reflects a reversible volumetric expansion of the polymer matrix upon oxidation, while the reverse process occurs during discharge, confirming the electromechanically active nature of the cathode.

Quantitative analysis of the average film height as a function of time (Figure S4a,d) shows a rapid and reproducible vertical expansion of 418 ± 32 nm (derived from four cycles) when the potential is increased to 2.2 V vs. Al/Al^{3+} (Figure S4e), which is attributed to the insertion of bulky Al-based anions required to maintain electroneutrality within the redox-active polymer network and the associated swelling. The excellent overlap of the height profiles over multiple cycles (4 cycles of 140 cycles are shown here) indicates that the X-PVMPT matrix can accommodate large volume changes without mechanical degradation, delamination, or loss of interfacial contact. The coupling between the electrochemical state and the mechanical response is further highlighted by the height-potential correlation plot (Figure S4c), which exhibits a clear hysteretic loop. This hysteresis indicates that although the ion insertion/extraction process is reversible, polymer-chain rearrangement and ion transport within the cross-linked matrix introduce kinetic and relaxation effects that slightly lag behind the potential sweep. Such behavior is known for organic polymer electrodes [52] and indicates energy dissipation associated with ion diffusion and structural relaxation during cycling. These results provide direct evidence that the electrochemical activity of the X-PVMPT cathode is intrinsically linked to its reversible volumetric response, underscoring its suitability for RAB applications despite mechanical deformation. We note that the spatiotemporal height map presented in Figure S4 was recorded after the electrode had reached a stable electrochemical state (after 140 cycles). By focusing on these later cycles, we characterize the intrinsic, nanoscopic swelling of the X-PVMPT network, allowing for the visualization of height transitions correlated with the applied potential, excluding high-strain transients and irreversible structural 'conditioning' - such as initial electrolyte wetting or polymer rearrangement - typically observed during the first redox cycles [6]. While the composite X-PVMPT electrode exhibits a uniform average surface roughness on the area scale ($S_a = 85 \pm 21$ nm, $S_z = 578 \pm 108$ nm, derived from full-scale maps), the porous nature of the composite - as evidenced by the SEM and AFM insets in Fig. 1 and Figure S2 - presents a challenging topography for continuous scanning. Friction forces in contact-mode AFM may perturb the polymer matrix during cycling. Therefore, the following studies were performed by recording vertical force-distance curves at each pixel, known as force-curve mappings, that effectively eliminates friction-induced artifacts and lateral tip-sample interactions. By performing high-speed force spectroscopy at every pixel, we obtain a more precise correlation between the electrochemical state and the local mechanical response of the polymer network.

3.3. Initial cycling behavior and electrode conditioning

A distinct increase of the redox peak currents in the CVs (Fig. 1c) was observed during the initial cycles of the X-PVMPT composite electrode, consistent with the activation behavior as previously reported for bulk electrochemical cycling of composite X-PVMPT electrodes [6]. While this initial phase is characterized by an increasing current, the subsequent cycles demonstrate stable electrochemical cyclability and quasi-reversible charge transfer, accompanied by stable height modulation. This conditioning phase, which has been previously described, can be attributed to synergistic mechanisms such as polymer matrix relaxation and electrolyte wetting. In addition, this condition phase may also promote stabilizing cation π-π* rearrangement processes within the polymer [4,6].

It should be noted that the initial electrochemical cycle of the X-PVMPT composite electrode could not be monitored via in situ ec-AFM, as the extensive structural reorganization and volume expansion caused a cantilever displacement likely driven by the abrupt nature of the height change or exceeding vertical range of the piezoelectric positioner (see Figure S5). This strong swelling behavior during the first cycle is attributed to an irreversible electro-activation or conditioning of the densely packed polymer matrix. Upon the first insertion of bulky Al-based anions ($AlCl_4^-$ and $Al_2Cl_7^-$), the cross-linked network undergoes a forced expansion, changing the polymer matrix during the first electrolyte-consuming formation cycle, generating the necessary free volume for subsequent ion transport. While previous studies have discussed this initial formation step in terms of ionic interactions and rearrangements within the ionic liquid electrolyte [20,53], our results provide direct evidence that this process is associated with a significant and previously unquantified volume expansion. This transition to a mechanical equilibrium was experimentally confirmed by the reproducibility of the height profiles (expansion/contraction behavior) in subsequent cycles, indicating that the irreversible conditioning was confined to the initial formation step. Consequently, the following cycles exhibit excellent reproducibility and a consistent, reversible height modulation. This stabilization of the mechanical response is a key indicator of the structural integrity of the X-PVMPT framework, suggesting that the polymer can accommodate strain over extended cycling without mechanical degradation.

The observed contact loss between AFM tip and sample during the first cycle, when the potential reaches a value of 2.0 V vs. Al/Al^{3+}in the cathodic scan, is clearly visible in the synchronized profiles (Figure S5), where the height signal plateaus and all mechanical parameters, including stiffness (k), Young's modulus (E), and adhesion force (F_{Adh}), abruptly drop to baseline levels. Despite this measurement distortion, the data provides crucial evidence of the extreme mechanical strain the framework can accommodate during its first formation cycle. The transition to a stabilized regime is confirmed by the highly reproducible expansion/contraction profiles observed in all subsequent cycles (Figs. 2–4 and S5), demonstrating the robust structural integrity and reversible height modulation of the stabilized X-PVMPT framework.

3.4. In situ spatiotemporal mapping using force-curve mappings

To directly probe the coupling between electrochemical activity and mechanical integrity of the X-PVMPT cathode, we performed in situ ec-AFM linescans ($x = 10$ μm) on the X-PVMPT composite electrode recording simultaneously the surface height changes, stiffness, deformation, electrochemical current and applied voltage. By performing such multiparametric analysis, we can analyze how ion insertion and extraction dynamically modulate both the structure and mechanical properties of the composite matrix.

As depicted in Fig. 2, the X-PVMPT composite electrode undergoes pronounced and reversible swelling upon polarization, accompanied by a modulation of the local stiffness (Figure S6), indicating that electrochemical charging not only drives volumetric expansion but also alters the mechanical properties of the polymer network. By focusing on these early cycles of the steady-state phase, we ensure that the observed amplitude reflects the reversible swelling process of the stabilized X-PVMPT network, effectively excluding transient effects from the initial

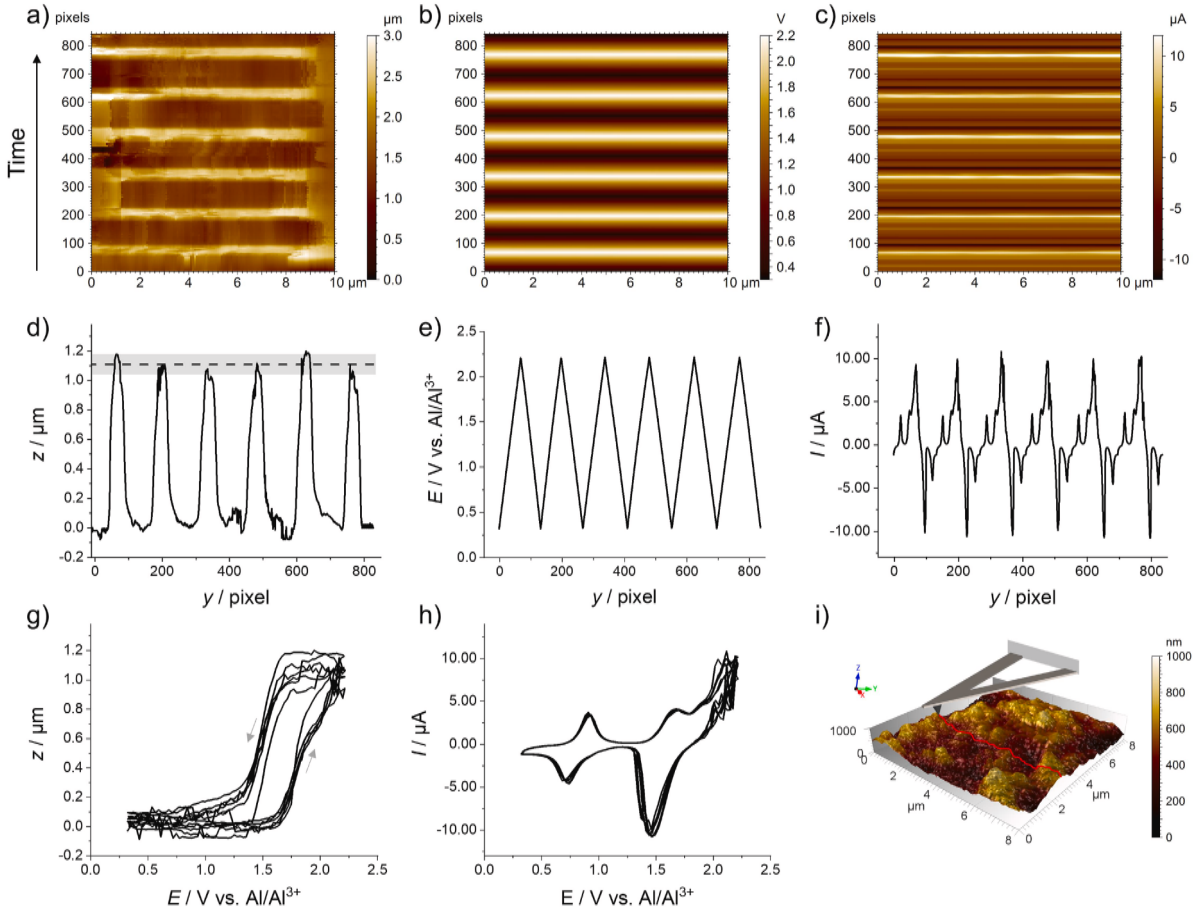

Fig. 2. In situ ec-AFM characterization of the X-PVMPT cathode during electrochemical cycling (cycles 5–10 are shown). a-c) Spatiotemporal maps showing the evolution of a) height, b) the applied electrochemical potential, and c) recorded macroscopic current as a function of time and space. The vertical axis represents the progression of multiple charge-discharge cycles, illustrating the synchronized mechanical and electrochemical response of the polymer matrix. d-f) Extracted line profiles along the y-direction (time axis) for d) height, e) potential, and f) current. g) Height-potential (z-E) hysteresis plot derived from the in situ mapping, demonstrating the reversible electro-chemo-mechanical response of the X-PVMPT composite electrode across multiple cycles. h) Corresponding CV extracted from the AFM data, showing two distinct redox couples characteristic of X-PVMPT in $AlCl_3$/[EMIm]Cl. i) 3D presentation of the topography (8 × 8 μm) illustrating the AFM cantilever path during force-curve acquisition.

activation phase (first cycle).

The spatiotemporal maps (Fig. 2a-c) provide a visualization of the electrode's cyclic volumetric response following the initial extreme activation period. The extracted height profiles (Fig. 2d) reveal a consistent and reversible swelling amplitude of approximately 1.1 ± 0.1 μm (n = 6 cycles, corresponding to 11.5% of the total film thickness). This vertical expansion correlates with the recorded current transients (Fig. 2f), confirming that the mechanical strain is a direct result of the faradaic processes. Specifically, the height-potential (z-E) hysteresis loops (Fig. 2g) demonstrate a steep swelling onset occurring above 1.4 V vs. Al/Al^{3+}, aligning with the oxidation peak observed in the corresponding AFM-derived CV (Fig. 2h), where the onset of the phenothiazine oxidation triggers the insertion of bulky $AlCl_4^-$ or $Al_2Cl_7^-$ anions and the subsequent expansion of the X-PVMPT framework. While Fig. 1a provides a general overview of the electrode surface, the 3D representation in Fig. 2i offers a more detailed perspective of the porous composite prior to electrochemical cycling. This multiparametric imaging extends beyond the purely topographic data shown in Figure S5 by correlating local stiffness with the redox state. By mapping the nanomechanical properties of the composite electrode, we observed that the volumetric expansion is coupled with an increase in stiffness associated to changes in the local Young's Modulus of the material (Figure S6) and a concurrent decrease in indentation deformation. Periodic fluctuations in deformation were observed, with values ranging from 0.05 to 0.50 μm. This expansion correlates with the insertion of ionic species into the composite matrix. During ion insertion (Figure S6b), the local stiffness increases, reaching peak values between 5 and 7 N/m, suggesting that electrochemical charging induces physical swelling that increases the local density of the composite. The derived modulus map confirms a transition toward a more rigid state, with values rising from 0.3 GPa to approximately 0.8–1.0 GPa at maximum insertion. These nanomechanical maps reveal a non-uniform mechanical change, which cannot be detected in standard topographic imaging. The observed reversible volume changes can be interpreted as a macroscopic manifestation of the Vegard strain, a concept traditionally used in solid-state chemistry but equally applicable to polymer networks, where it describes the linear relationship between the network volume and the concentration of inserted ions [54]. Unlike non-ionic contributions such as electrostriction or thermal expansion, the Vegard strain is directly proportional to the amount of charge stored, making it the primary signature of ion transport in the X-PVMPT system.

While the basic hysteretic behavior of the height was introduced in the previous section, the force-curve mappings constructed from sequential linescans now allow us to map this lag along the local mechanical stiffness. Correlating the swelling response with the electrochemical state further reveals a pronounced hysteresis in the height-potential relationship. This behavior indicates that, although ion insertion and extraction are electrochemically reversible, the associated

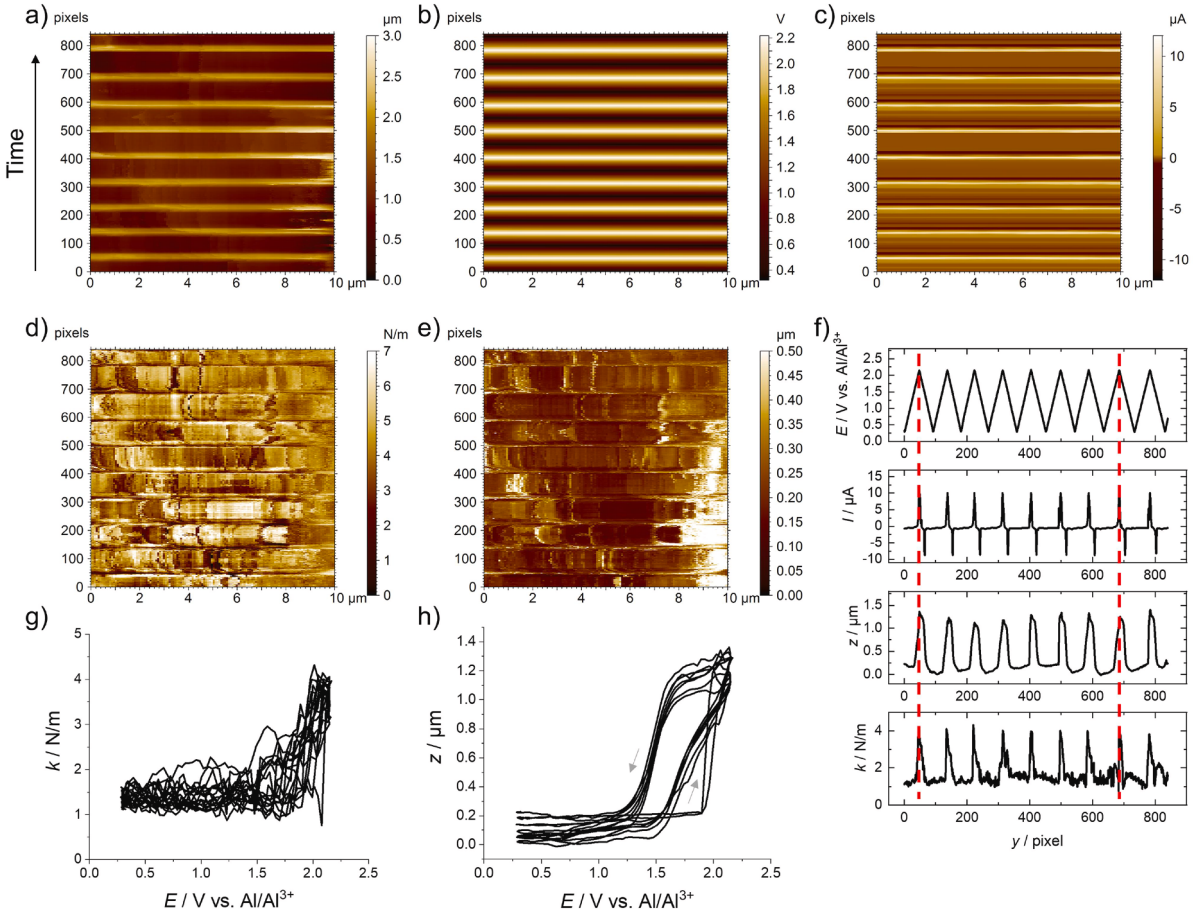

Fig. 3. In situ ec-AFM characterization of the X-PVMPT composite electrode during electrochemical cycling (cycles 50–59). a-c) Spatiotemporal maps showing the evolution of a) height, b) applied electrochemical potential, and c) recorded current as a function of time and space. d, e) 2D maps of mechanical properties showing d) the stiffness (k) and e) the deformation (δ). f) Extracted line profiles along the temporal (y) axis for potential, current, height, and stiffness. g) Stiffness-potential (k-E) and h) height-potential (z-E) hysteresis plots. The mechanical signatures remain highly reversible.

polymer chain rearrangement and ion transport within the cross-linked matrix involve kinetic and relaxation processes that do not instantaneously follow the potential sweep. This mechanical response confirms that the hysteresis is not simply a topographical artifact but inherent to the material's nanomechanical behavior**.** While ion transport is rate-limiting, the electrochemically stimulated conformational relaxation (ESCR) model [55] which attributes kinetic lag to chain rearrangement barriers, where the energy barrier for chain movement results in a delay [56], does not apply here. Height vs. charge analysis reveals that the hysteresis disappears confirming that expansion is directly coupled to ion insertion. Thus, the observed kinetic lag is not caused by conformational energy barriers, but is instead dictated by the transport-limited rate of charge moving through the polymer thickness.

To validate the temporal correlation of the data acquisition, the CV was reconstructed from the AFM auxiliary input channel, which recorded the analog current signal from the potentiostat in real-time (Figure S7a) and compared it to the direct potentiostat output (Figure S7b). The perfect correlation between the two plots confirms that the scanning probe does not interfere with the electrochemical response, ensuring a precise spatiotemporal linkage between faradaic redox processes and the observed mechanical swelling dynamics.

Following the characterization of the initial stabilization phase, we also evaluated the performance during extended cycling up to 160 cycles. By increasing the frequency of the individual force-curves, we captured multiple complete redox cycles within a single scan area to enhance the temporal throughput of the maps, allowing for the visualization of a higher number of complete electrochemical cycles and a more comprehensive overview of the performance of the electrode. Fig. 3 illustrates the in situ spatiotemporal response during cycles 50 to 59, where the X-PVMPT matrix continues to exhibit a robust and highly reversible electro-chemo-mechanical coupling. We identified this phase to last for about 120 cycles until the swelling amplitude starts to decay.

The spatiotemporal maps of height, potential, and current (Fig. 3a–c) confirm that the synchronized cyclic volumetric changes observed in early cycles remain intact after prolonged cycling (up to 140 cycles). Analysis of the extracted line profiles (Fig. 3f) reveals that the reversible swelling amplitude is nearly identical (swelling amplitude 1.2 μm ± 0.2 μm) to the initial cycles (cycles 5–10, Fig. 2), indicating that polymer network effectively accommodates the repeated strain due to bulky ion insertion without significant mechanical degradation at this stage which is in agreement with bulk electrochemical cycling data [6].

Recording the nanomechanical properties (stiffness and deformation, Fig. 3d and 4e) of the composite electrode during cycling, we identified the potential thresholds, where the polymer matrix transitions from a more flexible to a denser state. The stiffness-potential (*k-E*) and height-potential (*z-E*) hysteresis plots (Fig. 3g, h) show that the stiffness increase of the film remains tightly coupled to the swelling onset (1.4 V vs. Al/Al^{3+}). The polymer matrix undergoes a pronounced and reversible 4-fold increase in stiffness during oxidation (peaking at 4 N/m), primarily driven by insertion increasing the packing density and restricting the mobility of polymer chains. While these stiffness values are relatively high compared to pristine, soft polymer films, they are typical for composite electrodes where the addition of conductive carbon additives significantly enhances the overall mechanical rigidity of

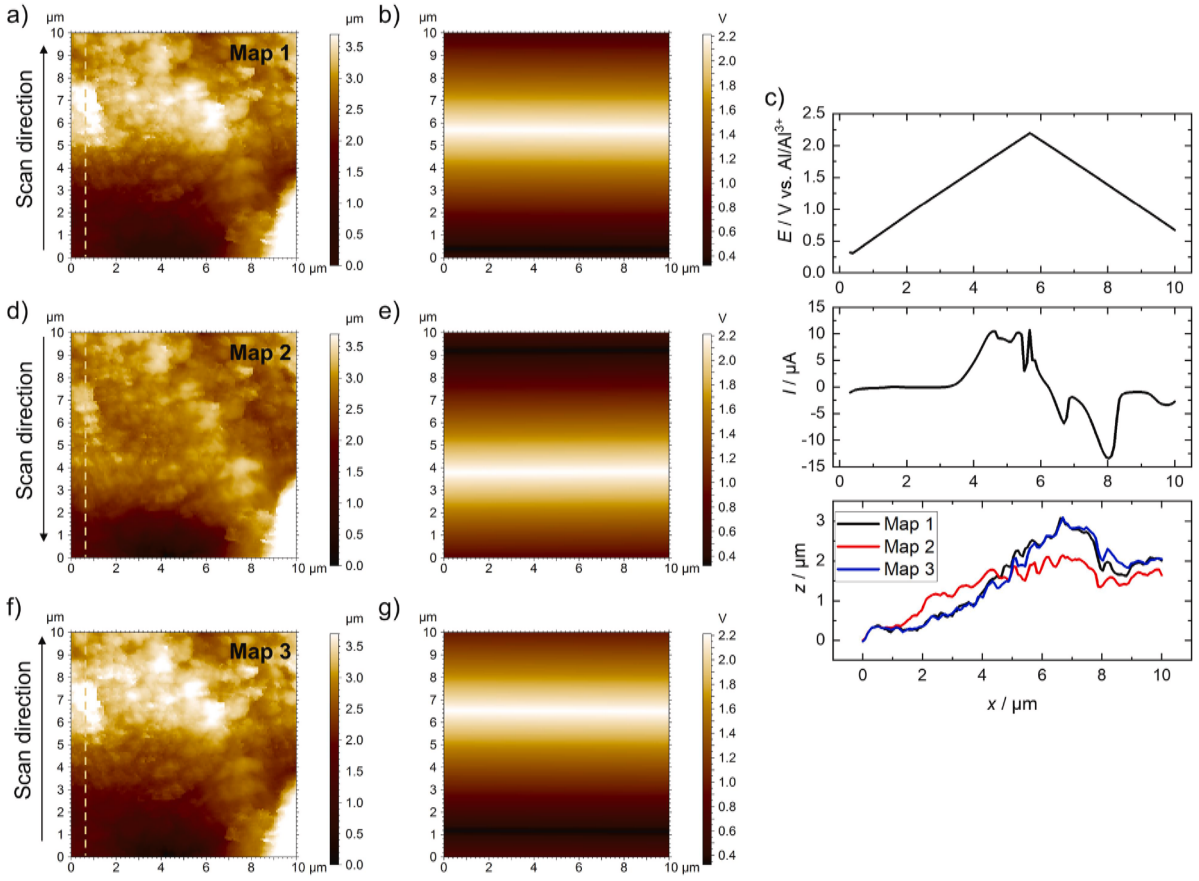

Fig. 4. In situ spatiotemporal mapping of the X-PVMPT cathode morphology during cycling (cycle 80–82). a, d, f) Sequential 2D height maps (map 1–3) obtained of a 10 × 10 μm area. The acquisition parameters were tuned to approximate the duration of single electrochemical cycle per frame, enabling the capture of a nearly full redox cycle (> 95%) within each image. b, e, g) Corresponding potential maps illustrating the linear voltage ramp applied during the acquisition of the respective height maps. c) Extracted line profiles along the dashed line in the fast scan direction (x) for the applied potential (top), recorded current (middle), and height evolution (bottom). E and I are displayed for the first cycle to ease the visualization, as the electrochemical response was highly reproducible despite the slight temporal offset at the start of the measurement.

the matrix. This behavior is consistent with the mechanical evolution observed in other redox-active polymers, where ion-induced cross-linking or counter-ion condensation leads to a significant increase in the elastic modulus during the doped state [57] as observed for example for polythiophenes and functionalized polythiophenes [58,59].

To investigate the long-term structural stability of the material under operating conditions, cycling was extended up to 150–159, as shown in Figure S8. While the temporal correlation between the potential sweep (Figure S8b) and the current response (Figure S8c) remains consistent with data shown in Fig. 3 (cycles 50–59 and 150–159), maintaining identical peak oxidation at 0.8 and 1.7 V, 2.0 V vs. Al/Al^{3+} and reduction potentials at 1.45 V vs. Al/Al^{3+} respectively, the corresponding height map (Figure S8a) reveals a clear decrease in expansion during cycling. The extracted line profiles (Figure S8f) show a reduced swelling amplitude of approximately 300 nm, a 75% reduction from the initial 1.2 μm expansion observed in the initial cycles of 5–10. This decrease in swelling amplitude became particularly evident starting from cycle 120, demonstrating that the mechanical evolution of the X-PVMPT composite electrode transitions through distinct stages. As the network establishes permanent ion channels, it transitions into a low-strain regime where the swelling amplitude drops from the intermediate 418 ± 32 nm recorded around cycle 140 down to 300 nm observed beyond cycle 150. Mathematically, this progressive stabilization represents a continuous 60% to 75% reduction in swelling amplitude, suggesting a gradual stabilization of the polymer network. Interestingly, the stiffness maps (k, Figure S8d) and the resulting k-E hysteresis plot (Figure S8g) indicate that the polymer matrix continues to undergo reversible stiffening upon oxidation, reaching values of up to 8 N/m. However, the height-potential (z-E) hysteresis (Figure S8h) shows a much narrower profile (swelling amplitude 0.28 ± 0.05 μm, n = 6 cycles) with a lower onset potential (ΔE = 0.1 V), suggesting that the cyclic volumetric changes have become more constrained.

Prolonged cycling of the X-PVMPT composite electrode leads to a pronounced modification of its voltammetric response. The voltammetric response of the X-PVMPT modified microelectrode (Figure S9) reveals the complex, multi-stage charge storage-mechanism, which is characteristic for conducting polymers in chloroaluminate ionic liquids [60]. The evolution of the CV profiles from the 10th to the 150th cycle reflects the transition of the polymer matrix from an initial as-prepared state to a stable, electrochemically conditioned network. As shown in Fig. 1, the initial CVs display two distinguishable redox couples: a lower-potential process centered around ~0.7 and 0.9 V and a redox pair at higher potentials (~1.4 and 1.7 V vs. Al/Al^{3+}). A notable increase in the peak current is observed between cycles 10 and 50 with the cathodic peak at ~1.4 V becoming sharper, suggesting a transition from a diffusion-limited process in the polymer matrix to a more kinetically driven regime. This is likely due to the structural relaxation of the cross-linked chains, which reduces the energetic barrier for ion transport. Upon extended cycling (e.g., cycle 150), both redox couples undergo changes in current intensity and peak shape. The symmetry between the anodic and cathodic scans improves, suggesting that the X-PVMPT film maintains structural integrity without significant

mechanical degradation or material dissolution in the ionic liquid. Most notably, the peak currents of the high-potential redox process significantly increase, with the anodic peak magnitude nearly doubling compared to the initial cycles (9.6 μA vs. 4.6 μA, Figure S9c). While the formation of a SEI is often associated with irreversible capacity loss and a decrease in peak currents, the observed current increase here suggests that any surface passivation in the chloroaluminate electrolyte is either negligible or outweighed by the progressive electro-activation of the polymer bulk. A similar trend is observed for the first redox peaks at 0.85 V vs. Al/Al^{3+}, which exhibit decreased peak currents and a slight broadening of the peaks. In contrast to bulk measurements [6], where differential capacity (dQ/dV) analysis indicates only uniform attenuation of redox features, the microelectrode reveals a split in electrochemical stability, highlighting changes in stability that are less obvious in macroscopic studies.

The preservation of high currents and the maintenance of peak symmetry (I_{pa} / I_{pc} ~ 1 indicative for quasi-reversible processes with a transfer coefficient of $\alpha = 0.5$) through 150 cycles show the robustness without notable degradation. Unlike non-crosslinked polymers [49], which may undergo dissolution [5] or significant swelling-induced mechanical failure in $AlCl_3$/[EMIm]Cl, the X-PVMPT framework maintains stable.

In situ ec-AFM measurements after more prolonged cycling (cycle 150–159) reveal a decrease in swelling amplitude from originally ~1.2 μm to ~0.3 μm during cycling. The cycled electrode exhibits reduced volumetric expansion with sustained and progressively enhanced faradaic performance driven by bulk electro-activation. This implies that microstructural rearrangements lead to a mechanically stabilized network that facilitates ion transport while requiring significantly less volumetric accommodation.

Such behavior suggests a transition from a diffusion-limited insertion mechanism in the early cycles to a kinetically improved regime after conditioning [56]. The observed reduction in swelling amplitude indicates that the ion transport pathways become more efficient, allowing for efficient charge compensation without the need for large-scale polymer chain displacement. EIS measurements were performed after different cycles to investigate the microstructural conditioning and the charge-transport kinetics. Figure S10 shows the Nyquist plots recorded at the modified microelectrode. The data reveals the decrease in charge-transfer between the 1st, 10th and 150th cycle. The associated charge-transfer resistance R_{ct} decreases significantly (from 12.2 ± 0.3 Ohm to 1.9 ± 0.1 Ohm) upon cycling, indicating that interfacial charge transfer is significantly improved over cycling. Concurrently, the low-frequency Warburg impedance region displays a slightly steeper slope for 150 cycles, which is indicative of accelerated, less diffusion-limited mass transport of the bulky chloroaluminate anions within the stabilized polymer matrix. Overall, we hypothesize that the irreversible structural reorganization during the initial phase lowers the internal resistance and establishes highly efficient ion-conduction pathways. To investigate the structural integrity and exclude mechanical failure over extended operation, post-cycling analysis was performed. As shown in Figure S11, SEM imaging, EDX analysis and AFM topography maps were performed to compare pristine organic composite electrodes with electrodes after 150 cycles. The data shows that the porous composite architecture remains intact, without any signs of fracturing, delamination, or significant material dissolution. The cycled electrodes were rinsed with 1,2-difluorobenzene prior to the transfer under Ar atmosphere to the SEM chamber. AFM imaging was conducted of the rinsed and dried samples in the glovebox. EDX analysis of the cycled electrode reveals prominent peaks for Al and Cl. These signals are attributed to residual chloroaluminate electrolyte trapped within the porous network of the composite polymer electrodes, confirming excellent electrolyte wetting and the successful retention of ion-conduction pathways after extended cycling.

To further probe the dynamics of the system, we employed mec-AFM. mec-AFM is an ec-AFM-derived technique, where an AC-modulation is applied to the applied sample potential while the AFM-tip is not electrically contacted and left floating. By demodulation, a separate imaging signal is obtained that contains the amplitude and phase of the electrochemical strain signal [45]. By superimposing a small AC voltage modulation of 100 mV onto the potential ramp during CV, we isolated the dynamic mechanical response of the X-PVMPT network. As shown in Figure S12, the electrode exhibits a potential-dependent electromechanical oscillation with amplitudes in the picometer range. This small-scale response represents the immediate breathing of the polymer surface in response to the fast AC-signal, which is different from the micrometer-scale DC swelling that builds up over much longer timescales. At a lower modulation frequency of 37 Hz (Figure S12a), a distinct increase in the oscillation amplitude is observed, peaking around the main redox transition potentials. While DC swelling reflects the cumulative volume change from bulk ion insertion, the picometer-scale mec-AFM signal captures only the instantaneous, dynamic, local strain induced by the rapid, small-amplitude AC-driven ion-exchange at the electrode-electrolyte interface. This correlates with the increased AC current (Figure S12c), suggesting that the polymer framework can dynamically respond to the rapid potential fluctuations through fast ion-exchange processes. However, when the frequency is increased to 77 Hz (Figure S12b), the mechanical response effectively disappears. This frequency-dependent attenuation points to a kinetic bottleneck. While bulky anion diffusion is likely a factor, the electronic conductivity of the X-PVMPT matrix also reaches a threshold at higher frequencies. Consequently, the signal attenuation at 77 Hz arises from the ionic diffusion and electronic transport constraints, effectively ruling out structural relaxation, which is too fast to be the limiting factor.

3.5. *In situ nanomechanical mapping of 2D swelling dynamics*

To move beyond the temporal insights provided by linescan analysis, we performed in situ 2D force-curve mappings (10 × 10 μm area) as shown in Fig. 4. The force-curve acquisition frequency was optimized to approximate the duration of the electrochemical sweep. In this configuration, each AFM frame captures approx. >95% of a single electrochemical cycle, providing spatially resolved insight into the structural evolution across the entire potential window. It should be noted that because the individual force-curve duration is dynamically influenced by the local topography and the vertical swelling of the X-PVMPT, a minor temporal offset cannot be avoided between the completion of the AFM frame and the CV cycle. Despite this, the approach provides a spatially resolved view of the structural evolution, rather than a single-line observation.

The height maps (Fig. 4a, d, f) reveal a pronounced and reproducible potential-dependent reversible volume change across the entire scanned area. The corresponding potential profiles (Fig. 4b, e, g) are critical for interpreting these images, as they provide a direct temporal-to-potential reference. Each image captures both the anodic and cathodic sweep, and lateral height profiles extracted along the fast scan direction (Fig. 4c, bottom) show the increase in height with progressing potential, reaching a maximum amplitude of approximately 1.1 μm (cycle 80–82). This result is in excellent agreement with the previous linescan measurements, confirming that the observed mechanical deformation is not a localized artifact but a representative bulk property of the X-PVMPT composite electrode, since the entire surface responds to the potential sweep validating the hypothesis that swelling is driven by a global ion-pairing mechanism, where the bulky $AlCl_4^-$ anions insert into the porous polymer network.

The three consecutive maps (map 1–3) display highly consistent behavior in terms of both the absolute amplitude and the shape of the height evolution along the lateral direction. Minor variations in the maximum height (on the order of 10–15%) can be attributed to small-scale heterogeneities in the microstructure.

The consistent reproduction of the swelling amplitude across the

three maps confirms the high degree of mechanical integrity within the composite, demonstrating that the polymer network remains effectively interconnected and adhered to the carbon matrix despite the volumetric strain.

3.6. *Electrochemical response and mechanical evolution in the absence of aluminum species*

To assess whether the pronounced nanomechanical response observed previously is associated with aluminum-ion insertion or whether it could partially arise from nonspecific effects such as electrolyte uptake or polymer relaxation we performed a control experiment using an aluminum-free ionic liquid electrolyte, motivated by the need to evaluate the origin of the measured potential-dependent volumetric expansion (Fig. 5).

The X-PVMPT cathode was cycled in a mixture of [EMIm]Cl and ethylene glycol, which provides comparable ionic conductivity and wetting behavior but contains no aluminum species [48]. Under otherwise identical electrochemical and AFM conditions, the electrode exhibited only negligible thickness variations. While these minor fluctuations remained largely reversible - similar to the behavior observed in the chloroaluminate-containing Al system - the swelling amplitude (0.13 ± 0.02 µm, $n = 8$ cycles) was at least one order of magnitude smaller than during active ion insertion.

In general, the interpretation of strain signals is complicated by various non-ionic contributions, such as thermal expansion, electrostriction and electrostatic forces, which can obscure the k, which describes the linear coupling between the polymer network volume and the concentration of inserted species, associated with ion transport. The strongly suppressed mechanical response in the absence of chloroaluminate ions demonstrates that solvent uptake, electrolyte-induced plasticization, or purely electrostatic charging effects contribute only to a small extent to the overall dimensional changes of the polymer film. Instead, the results indicate that the large and reversible swelling observed originates predominantly from the electrochemical insertion and extraction of aluminum-based species.

As expected, and illustrated in Fig. 5, the absence of aluminum-based species leads to a significant suppression of the voltammetric redox features, with the current response (Fig. 5c, g) being dominated by capacitive charging and electrolyte decomposition above 1.8 V vs. Al/Al^{3+}. While an aluminum wire was used as the CE/RE for experimental consistency, the lack of Al-species in the electrolyte prevents the formation of a defined Al/Al^{3+} Nernstian equilibrium. Consequently, the electrode serves only as a pseudo-reference and does not act as a source for aluminum insertion. The current response is dominated by a continuously increasing background current characteristic of double-layer charging and non-faradaic polarization processes. The lack of corresponding cathodic features upon reversing the potential supports the interpretation of this process as irreversible electrolyte decomposition. The absence of defined redox features confirms that the X-PVMPT composite does not undergo redox transitions in the absence of aluminum species. This observation further validates that the pronounced redox couples observed in the Al-containing electrolyte originate from reversible insertion and extraction of aluminum-based ions.

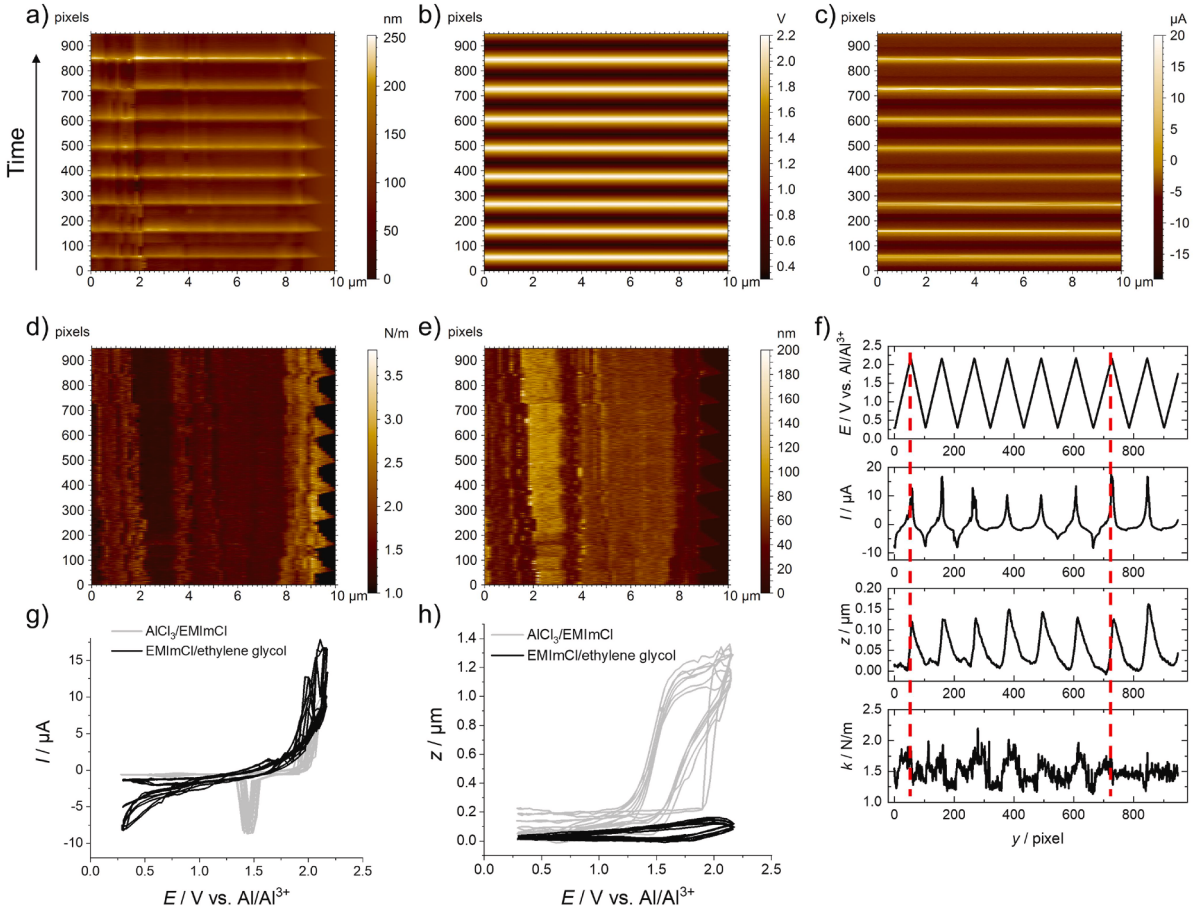

Fig. 5. Control experiment in aluminum-free electrolyte. a–e) In situ ec-AFM spatiotemporal maps using force-curve mappings showing a) height, b) applied potential, c) current, d) stiffness (k), and e) deformation during cycling of the X-PVMPT cathode in an Al-free [EMIm]Cl/ethylene glycol mixture. f) Corresponding line profiles extracted from the maps, highlighting the suppressed current (I) and minimal height changes (z) compared to Al-containing electrolytes. g) Comparison of CVs and h) height-potential hysteresis plot between the $AlCl_3$ /[EMIm]Cl (grey) and the Al-free (black) electrolytes.

Correspondingly, the height and line profiles (Fig. 5a, f) reveal that the cyclic volume changes are reduced by more than an order of magnitude without faradaic ion-pairing. The nearly negligible hysteresis in Fig. 5h confirms that the swelling observed in the main experiments is a consequence of reversible aluminum-ion insertion, rather than a non-specific electrolyte effect.

3.7. EQCM-D studies

While ec-AFM provides localized, spatiotemporal nanomechanical data, EQCM-D provides insight into mass change and viscoelastic changes of the X-PVMPT composite electrode. To validate the findings obtained via ec-AFM, we performed EQCM-D measurements, which allow for the simultaneous monitoring of apparent mass change (Δm), dissipation (ΔD) and the resonance half-bandwidth ($\Delta\Gamma$) during electrochemical cycling. The 3rd overtone ($n = 3$) was selected for data analysis, which offers optimal sensitivity to the viscoelastic properties of the X-PVMPT film while maintaining a robust resonance signal, as shown in Fig. 6a.

The investigation starts with monitoring the electrode immersed in electrolyte during a 30-minute period at OCV. No changes in frequency and/or dissipation are observed, indicating that no spontaneous reactions/swelling take place. During subsequent electrochemical cycling using cyclic voltammetry, we observe highly reversible changes in frequency and dissipation signals that coincide with the electrochemical oxidation/reduction reactions. The onset of the oxidation reaction aligns with a frequency decrease and a drop in dissipation and resonance half-bandwidth. Correspondingly, both signals reverse during reduction. The observations support an anion-driven charge storage mechanism, which leads to an apparent mass-uptake during the anodic cycle/oxidation (equivalent to frequency drop). At the same time, the drops in dissipation and resonance half-bandwidth are in agreement with the stiffening upon anion-uptake. The fully oxidized, dicationic state of X-PVMPT forms a more compact and rigid configuration due to strong electrostatic interaction with the $AlCl_4^-/Al_2Cl_7^-$ anions, e.g., by suppressing the viscous motion of the polymer chains. This macro-scale stiffening observed by EQCM-D is in excellent agreement with the increase in stiffness and Young's Modulus identified via local AFM force-mapping, providing conclusive evidence of the electrochemically induced stiffening mechanism. Our EQCM-D investigation supports that this process is highly reversible. The results are further illustrated in a single CV cycle (3rd cycle), where the apparent surface mass density increase/decrease aligns with the anodic/cathodic peaks, respectively (Fig. 6b). It should be noted that the irreversible anodic and cathodic features which correspond to side reactions in the EQCM cell do not lead to detectable changes in the measured frequency.

4. Conclusion

In this work, we employed cyclic voltammetry, in situ ec-AFM and EQCM-D to investigate the nanoscale structural and mechanical evolution of a cross-linked phenothiazine-based polymer (X-PVMPT) composite as positive electrode during operation in $AlCl_3$/[EMIm]Cl against an Al metal negative electrode. We could show that in situ ec-AFM successfully visualized the dynamic electro-chemo-mechanical behavior of the X-PVMPT positive electrode during aluminum-ion insertion and extraction. The observed coupling between electrochemical activity and mechanical deformation is an intrinsic property of the X-PVMPT cathode in a RAB. The combined electrochemical and morphological analyses revealed that the insertion and extraction of $AlCl_4^-$ / $Al_2Cl_7^-$ anions induce a pronounced, reversible swelling and relaxation response within the polymer matrix, which is tightly correlated and coupled to its redox state. Quantitative analysis identified three distinct mechanical phases during cycling: initial conditioning (first cycle), steady-state cycling range (cycles 2–120), long-term stabilization (up to 160 cycles). While initial cycles were marked by significant electro-activation and volumetric strain even exceeding the measurement range in the first cycle, the X-PVMPT composite electrode achieved a stable mechanical equilibrium starting at the second cycle. By utilizing spatiotemporal linescan maps, we successfully visualized the real-time synchronization between electrochemical redox transitions and vertical swelling, identifying a distinct conditioning phase

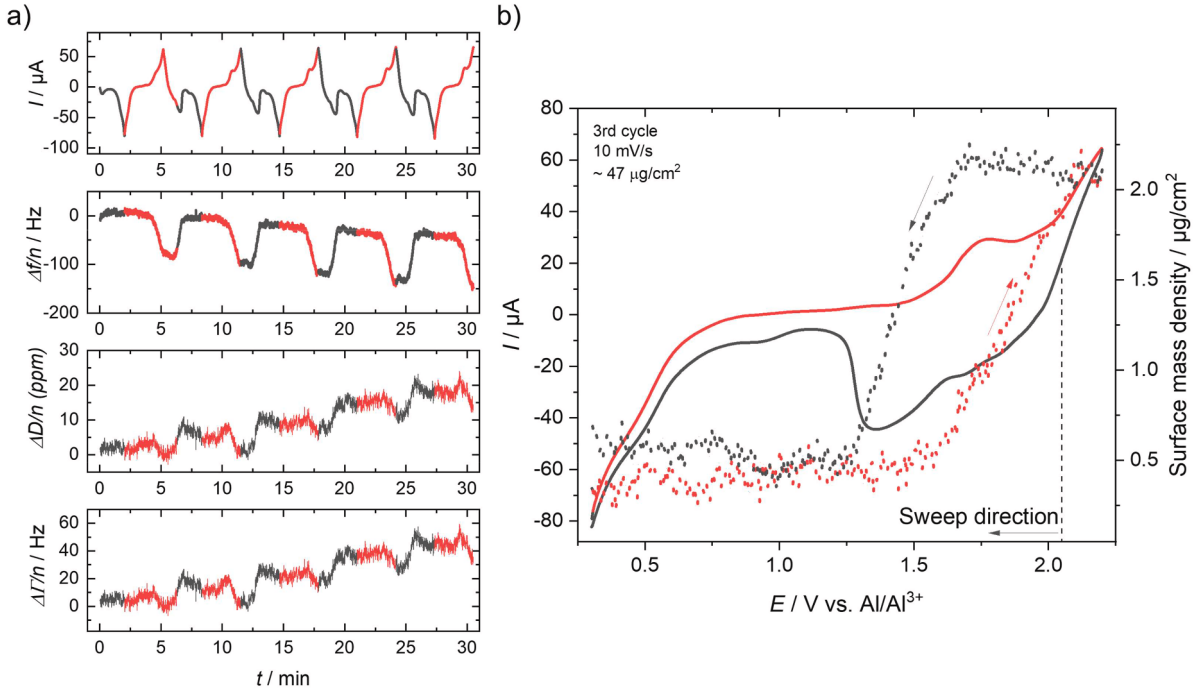

Fig. 6. a) In situ EQCM-D characterization of the X-PVMPT composite electrode during electrochemical cycling at a scan rate of 10 mV/s. From top to bottom: I, normalized frequency shift (Δf/n), dissipation change (ΔD/n), and half-bandwidth shift (ΔΓ/n). b) CV and apparent surface mass density change (derived from frequency change) of the X-PVMPT composite electrode. Signals in the cathodic half-cycle in black, anodic half-cycle in red.

where the polymer matrix reorganizes to accommodate bulky chloroaluminate ions.

Nanomechanical mappings confirmed that height changes of 1.1 ± 0.1 μm (equivalent to 11.5% of total film thickness) μm are a representative bulk property of the interconnected composite rather than a localized artifact. The volumetric expansion is coupled with a reversible 4-fold increase in stiffness and a transition toward a more rigid state with a Young's Modulus rising to 0.8–1.0 GPa at maximum ion insertion. EQCM-D analysis of the dissipation and resonance half-bandwidth provided macroscopic validation of this stiffening, showing that the fully oxidized state of X-PVMPT forms a compact, rigid configuration that suppresses polymer chain flexibility. Extended cycling demonstrated the structural durability of the cross-linked network, which transitioned from an initial high-expansion regime (~1.2 μm) to a low-strain state (0.3 – 0.4 μm, up to 60–75% decrease in the swelling amplitude) in the cycle range of 150–159. This transition occurs with sustained and progressively enhanced faradaic currents driven by bulk electro-activation without any significant performance loss. Frequency-dependent mec-AFM studies indicate relaxation processes inherent to the ion-pairing mechanism. These multi-dimensional studies, validated by aluminum-free control experiments resulting in the absence of redox features and a significantly reduced mechanical response, giving for the first time insight into the swelling behavior and the role of redox-induced Al-based anion insertion of X-PVMPT. The mechanical stability, and structural flexibility, makes X-PVMPT an ideal polymer for RABs. Future studies will focus on the kinetics of the redox processes driving insertion/desertion processes.

CRediT authorship contribution statement

Sven Daboss: Conceptualization, Data Curation, Formal Analysis, Investigation, Writing - Original Draft, Review & Editing. **Eva Bräutigam:** X-PVMPT slurry preparation, EIS measurement, Writing – Review & Editing. **Birgit Esser:** Conceptualization, Funding Acquisition, Review & Editing. **Tobias Cramer:** Support with mec-AFM measurements, Review & Editing. **Mete Batuhan Durukan:** EQCM-D measurements and analysis, **Simon Fleischmann:** Review & Editing, **Christine Kranz:** Conceptualization, Supervision, Funding Acquisition, Writing – Original Draft, Writing – Review & Editing.

Declaration of competing interest

The authors declare that they have no known competing financial interests or personal relationships that could have appeared to influence the work reported in this paper.

Acknowledgements

We thank Dr. Philipp Penert (Ulm University) for providing X-PVMPT. We thank the Core Facility EMMA at Ulm University for providing access to FIB/SEM instrumentation. This work contributes to the research performed at CELEST (Center for Electrochemical Energy Storage Ulm - Karlsruhe) and was funded by the Deutsche Forschungsgemeinschaft (DFG, German Research Foundation) under Germany's Excellence Strategy – EXC 2154 – Project number 390874152 (POLiS Cluster of Excellence), as well as under project number 441215516 (SPP 2248 "Polymer-based batteries). M.B.D. acknowledges funding from the Alexander von Humboldt Foundation. S.F. acknowledges support from the German Federal Ministry of Research, Technology and Space (BMFTR) in the NanoMatFutur program (03XP0423).

Supplementary materials

Supplementary material associated with this article can be found, in the online version, at doi:10.1016/j.electacta.2026.149354.

Data availability

The data that support the findings of this study are openly available in Zenodo DOI: 10.5281/zenodo.18186105, reference number 509.

References

[1] G.A. Elia, K. Marquardt, K. Hoeppner, S. Fantini, R. Lin, E. Knipping, W. Peters, J. Drillet, S. Passerini, R. Hahn, An overview and future perspectives of aluminum batteries, Adv. Mater. 28 (2016) 7564–7579, https://doi.org/10.1002/adma.201601357.

[2] F. Wu, H. Yang, Y. Bai, C. Wu, Paving the path toward reliable cathode materials for aluminum-ion batteries, Adv. Mater. 31 (2019) 1–18, https://doi.org/10.1002/adma.201806510.

[3] Y. Zhang, S. Liu, Y. Ji, J. Ma, H. Yu, Emerging nonaqueous aluminum-ion batteries: challenges, status, and perspectives, Adv. Mater. 30 (2018) 1706310, https://doi.org/10.1002/adma.201706310.

[4] M. Kolek, F. Otteny, P. Schmidt, C. Mück-Lichtenfeld, C. Einholz, J. Becking, E. Schleicher, M. Winter, P. Bieker, B. Esser, Ultra-high cycling stability of poly (vinylphenothiazine) as a battery cathode material resulting from π–π interactions, Energy Environ. Sci. 10 (2017) 2334–2341, https://doi.org/10.1039/C7EE01473B.

[5] V. Perner, D. Diddens, F. Otteny, V. Küpers, P. Bieker, B. Esser, M. Winter, M. Kolek, Insights into the solubility of poly(vinylphenothiazine) in carbonate-based battery electrolytes, ACS. Appl. Mater. Interfaces. 13 (2021) 12442–12453, https://doi.org/10.1021/acsami.0c20012.

[6] G. Studer, A. Schmidt, J. Büttner, M. Schmidt, A. Fischer, I. Krossing, B. Esser, On a high-capacity aluminium battery with a two-electron phenothiazine redox polymer as a positive electrode, Energy Environ. Sci. 16 (2023) 3760–3769, https://doi.org/10.1039/D3EE00235G.

[7] R. Wessling, H. Koger, F. Otteny, M. Schmidt, A. Semmelmaier, B. Esser, Unlocking twofold oxidation in phenothiazine polymers for application in symmetric all-organic anionic batteries, ACS. Appl. Polym. Mater. 6 (2024) 7956–7968, https://doi.org/10.1021/acsapm.4c00500.

[8] P. Poizot, J. Gaubicher, S. Renault, L. Dubois, Y. Liang, Y. Yao, Opportunities and challenges for organic electrodes in electrochemical energy storage, Chem. Rev. 120 (2020) 6490–6557, https://doi.org/10.1021/acs.chemrev.9b00482.

[9] B. Esser, F. Dolhem, M. Becuwe, P. Poizot, A. Vlad, D. Brandell, A perspective on organic electrode materials and technologies for next generation batteries, J. Power. Sources 482 (2021) 228814, https://doi.org/10.1016/j.jpowsour.2020.228814.

[10] S. Muench, A. Wild, C. Friebe, B. Häupler, T. Janoschka, U.S. Schubert, Polymer-based organic batteries, Chem. Rev. 116 (2016) 9438–9484, https://doi.org/10.1021/acs.chemrev.6b00070.

[11] Z. Huang, X. Du, M. Ma, S. Wang, Y. Xie, Y. Meng, W. You, L. Xiong, Organic cathode materials for rechargeable aluminum-ion batteries, ChemSusChem 16 (2023) e202202358, https://doi.org/10.1002/cssc.202202358.

[12] Y. Chen, K. Fan, Y. Gao, C. Wang, Challenges and perspectives of organic multivalent metal-ion batteries, Adv. Mater. 34 (2022) 1–16, https://doi.org/10.1002/adma.202200662.

[13] Q. Guo, H. Xu, X. Chu, X. Huang, M. Yu, X. Feng, Structural codes of organic electrode materials for rechargeable multivalent metal batteries, Chem. Soc. Rev. 54 (2025) 4035–4086, https://doi.org/10.1039/D4CS01072H.

[14] P. Poizot, F. Dolhem, J. Gaubicher, Progress in all-organic rechargeable batteries using cationic and anionic configurations: toward low-cost and greener storage solutions? Curr. Opin. Electrochem. 9 (2018) 70–80, https://doi.org/10.1016/j.coelec.2018.04.003.

[15] M. Tang, H. Li, E. Wang, C. Wang, Carbonyl polymeric electrode materials for metal-ion batteries, Chin. Chem. Lett. 29 (2018) 232–244, https://doi.org/10.1016/j.cclet.2017.09.005.

[16] X. Peng, A. Baktash, Y. Huang, N. Alghamdi, J. You, J. Ning, R. Xin, L. Hao, T. Qiu, B. Wang, L. Zhi, L. Wang, B. Luo, Multi-redox covalent organic frameworks for aluminium organic batteries, Energy Storage Mater. 71 (2024) 103674, https://doi.org/10.1016/j.ensm.2024.103674.

[17] E. Fuentes-Mendoza, M. Talari, E. Zemlyanushin, R. Cordoba, N. Sabi, S. Dsoke, Navigating the challenges of rechargeable aluminum battery research: material instabilities, technical hurdles, and future directions, ChemElectroChem 12 (2025) e202400705, https://doi.org/10.1002/celc.202400705.

[18] T. Ma, A.D. Easley, R.M. Thakur, K.T. Mohanty, C. Wang, J.L. Lutkenhaus, Nonconjugated redox-active polymers: electron transfer mechanisms, energy storage, and chemical versatility, Annu. Rev. Chem. Biomol. Eng. 14 (2023) 187–216, https://doi.org/10.1146/annurev-chembioeng-092220-111121.

[19] M. Ademmer, P.-H. Su, L. Dodell, J. Asenbauer, M. Osenberg, A. Hilger, J.-K. Chang, I. Manke, M. Neumann, V. Schmidt, D. Bresser, Unveiling the impact of cross-linking redox-active polymers on their electrochemical behavior by 3D imaging and statistical microstructure analysis, J. Phys. Chem. C 127 (2023) 19366–19377, https://doi.org/10.1021/acs.jpcc.3c04162.

[20] L. Dodell, M. Neumann, M. Osenberg, A. Hilger, G. Studer, B. Esser, I. Manke, V. Schmidt, Quantifying local heterogeneities in the 3D morphology of X-PVMPT battery electrodes based on FIB-SEM measurements, ACS. Mater. Lett. 7 (2025) 1914–1921, https://doi.org/10.1021/acsmaterialslett.4c01552.

[21] N. Ortlieb, B. Tengen, V. Perner, M. Winter, B. Esser, P. Bieker, A. Fischer, Improving the capacity retention of poly(vinylphenothiazine) as battery electrode material by pore size engineering of porous N -doped carbon nanospheres as

conductive additive, Adv. Funct. Mater. 35 (2025) 1–16, https://doi.org/10.1002/adfm.202422302.
[22] X. Luo, J. Wang, M. Dooner, J. Clarke, Overview of current development in electrical energy storage technologies and the application potential in power system operation, Appl. Energy 137 (2015) 511–536, https://doi.org/10.1016/j.apenergy.2014.09.081.
[23] A. Noori, M.F. El-Kady, M.S. Rahmanifar, R.B. Kaner, M.F. Mousavi, Towards establishing standard performance metrics for batteries, supercapacitors and beyond, Chem. Soc. Rev. 48 (2019) 1272–1341, https://doi.org/10.1039/c8cs00581h.
[24] W. Guan, Z. Huang, W. Wang, W.L. Song, J. Tu, Y. Luo, H. Lei, M. Wang, S. Jiao, The negative-charge-triggered "dead zone" between electrode and current collector realizes ultralong cycle life of aluminum-ion batteries, Adv. Mater. 35 (2023) 1–13, https://doi.org/10.1002/adma.202205489.
[25] H. Sun, W. Wang, Z. Yu, Y. Yuan, S. Wang, S. Jiao, A new aluminium-ion battery with high voltage, high safety and low cost, Chem. Commun. 51 (2015) 11892–11895, https://doi.org/10.1039/C5CC00542F.
[26] T. Dutta, J.M. Gladis, Recent developments on electrode materials and electrolytes for aluminium-ion batteries, J. Energy Storage 86 (2024) 111287, https://doi.org/10.1016/j.est.2024.111287.
[27] W.Y. Tsai, R. Wang, S. Boyd, V. Augustyn, N. Balke, Probing local electrochemistry via mechanical cyclic voltammetry curves, Nano Energy 81 (2021) 105592, https://doi.org/10.1016/j.nanoen.2020.105592.
[28] D. Sauerteig, S. Ivanov, H. Reinshagen, A. Bund, Reversible and irreversible dilation of lithium-ion battery electrodes investigated by in-situ dilatometry, J. Power. Sources 342 (2017) 939–946, https://doi.org/10.1016/j.jpowsour.2016.12.121.
[29] H. Tavassol, E.M.C. Jones, N.R. Sottos, A.A. Gewirth, Electrochemical stiffness in lithium-ion batteries, Nat. Mater. 15 (2016) 1182–1187, https://doi.org/10.1038/nmat4708.
[30] Z.J. Schiffer, J. Cannarella, C.B. Arnold, Strain derivatives for practical charge rate characterization of lithium ion electrodes, J. Electrochem. Soc. 163 (2016) A427–A433, https://doi.org/10.1149/2.0091603jes.
[31] H. Jiang, J. Chen, X. Li, Z. Jin, T. Chen, J. Liu, D. Li, A comprehensive review of In situ measurement techniques for evaluating the electro-chemo-mechanical behaviors of battery electrodes, Molecules 29 (2024) 1873, https://doi.org/10.3390/molecules29081873.
[32] E. Smela, N. Gadegaard, Volume change in polypyrrole studied by atomic force microscopy, J. Phys. Chem. B 105 (2001) 9395–9405, https://doi.org/10.1021/jp004126u.
[33] M.R. Gandhi, P. Murray, G.M. Spinks, G.G. Wallace, Mechanism of electromechanical actuation in polypyrrole, Synth. Met. 73 (1995) 247–256, https://doi.org/10.1016/0379-6779(95)80022-0.
[34] B. Roschning, J. Weissmüller, Stress-charge coupling coefficient for thin-film polypyrrole actuators – Investigation of capacitive ion exchange in the oxidized state, Electrochim. Acta 318 (2019) 504–512, https://doi.org/10.1016/j.electacta.2019.05.166.
[35] K.-G. Kim, G.H. Park, D.O. Agumba, S.Y. Kim, In-situ measurement of drying and electrochemical-cycling-induced mechanical behavior and delamination of polypyrrole electrodes for energy storage applications, Surf. Interfaces. 34 (2022) 102297, https://doi.org/10.1016/j.surfin.2022.102297.
[36] T. Brendel, M. Janzen, M. Müller, W. Bauer, D. Kramer, R. Mönig, The dynamics of the structure of composite electrodes during their operation in lithium-ion batteries, Energy Technol. 13 (2025) 2500106, https://doi.org/10.1002/ente.202500106.
[37] S. Mück, D. Kramer, K. Palanisamy, C. Kranz, R. Mönig, Mechanical stress reveals asymmetry of sodiation and desodiation of hard carbon, ChemSusChem 18 (2025) e202501272, https://doi.org/10.1002/cssc.202501272.
[38] R. Kempaiah, G. Vasudevamurthy, A. Subramanian, Scanning probe microscopy based characterization of battery materials, interfaces, and processes, Nano Energy 65 (2019) 103925, https://doi.org/10.1016/j.nanoen.2019.103925.
[39] Z. Zhang, S. Said, K. Smith, R. Jervis, C.A. Howard, P.R. Shearing, D.J.L. Brett, T. S. Miller, C.B In, Situ electrochemical atomic force microscopy: a critical review, Adv. Energy Mater. 11 (2021) 2101518, https://doi.org/10.1002/aenm.202101518.
[40] M. Wang, Z. Song, J. Bi, H. Li, M. Xu, Y. Gong, Y. Zhou, Y. Zhao, K. Yang, Probing interfacial electrochemistry by in situ atomic force microscope for battery characterization, Batter. Energy 2 (2023) 1–20, https://doi.org/10.1002/bte2.2023006.
[41] R.B. Lewis, A. Timmons, R.E. Mar, J.R. Dahn, In situ AFM measurements of the expansion and contraction of amorphous Sn-Co-C films reacting with lithium, J. Electrochem. Soc. 154 (2007) A213, https://doi.org/10.1149/1.2429042.
[42] N. Balke, S. Jesse, A.N. Morozovska, E. Eliseev, D.W. Chung, Y. Kim, L. Adamczyk, R.E. García, N. Dudney, S.V. Kalinin, Nanoscale mapping of ion diffusion in a lithium-ion battery cathode, Nat. Nanotechnol. 5 (2010) 749–754, https://doi.org/10.1038/nnano.2010.174.
[43] S. Daboss, N. Franke, B. Fraboni, C. Kranz, T. Cramer, Modulated electrochemical force microscopy: investigation of sodium-ion transport at hard carbon composite anodes, J. Microsc. 302 (2026) 17–28, https://doi.org/10.1111/jmi.13417.
[44] F. Bonafè, C. Dong, G.G. Malliaras, T. Cramer, B. Fraboni, Subsurface profiling of ion migration and swelling in conducting polymer actuators with modulated electrochemical atomic force microscopy, ACS. Appl. Mater. Interfaces. 16 (2024) 36727–36734, https://doi.org/10.1021/acsami.4c08459.
[45] F. Bonafè, F. Decataldo, T. Cramer, B. Fraboni, Ionic solvent shell drives electroactuation in organic mixed Ionic-electronic conductors, Adv. Sci. 11 (2024) 2308746, https://doi.org/10.1002/advs.202308746.
[46] R. Wang, J.B. Mitchell, Q. Gao, W.Y. Tsai, S. Boyd, M. Pharr, N. Balke, V. Augustyn, Operando Atomic Force microscopy reveals mechanics of structural water driven battery-to-pseudocapacitor transition, ACS. Nano 12 (2018) 6032–6039, https://doi.org/10.1021/acsnano.8b02273.
[47] T. Proksch, V.J. Musicó, S. Saeed, W. Tsai, V. Augustyn, N. Balke, Electrochemical strain measurements with atomic force microscopy: principles and applications, ACS Electrochem. 2 (2026) 92–100, https://doi.org/10.1021/acselectrochem.5c00411.
[48] G. Saravanan, S. Mohan, Nucleation of copper on mild steel in copper chloride (CuCl2·2H2O)–1-ethyl-3-methylimidazolium chloride [EMIM]Cl–ethylene glycol (EG) ionic liquid, New. J. Chem. 37 (2013) 2564, https://doi.org/10.1039/c3nj00245d.
[49] F. Otteny, M. Kolek, J. Becking, M. Winter, P. Bieker, B. Esser, Unlocking full discharge capacities of poly(vinylphenothiazine) as battery cathode material by decreasing polymer mobility through cross-linking, Adv. Energy Mater. 8 (2018) 1–8, https://doi.org/10.1002/aenm.201802151.
[50] J.L. Hutter, J. Bechhoefer, Calibration of atomic-force microscope tips, Rev. Sci. Instrum. 64 (1993) 1868–1873, https://doi.org/10.1063/1.1143970.
[51] J. Schindelin, I. Arganda-Carreras, E. Frise, V. Kaynig, M. Longair, T. Pietzsch, S. Preibisch, C. Rueden, S. Saalfeld, B. Schmid, J.-Y. Tinevez, D.J. White, V. Hartenstein, K. Eliceiri, P. Tomancak, A. Cardona, Fiji: an open-source platform for biological-image analysis, Nat. Methods 9 (2012) 676–682, https://doi.org/10.1038/nmeth.2019.
[52] X. Wang, H. Dong, A.E. Lakraychi, Y. Zhang, X. Yang, H. Zheng, X. Han, X. Shan, C. He, Y. Yao, Electrochemical swelling induced high material utilization of porous polymers in magnesium electrolytes, Mater. Today 55 (2022) 29–36, https://doi.org/10.1016/j.mattod.2022.04.010.
[53] B. Esser, I.H. Morhenn, M. Keis, Phenothiazine polymers as versatile electrode materials for next-generation batteries, Accounts Mater. Res. 6 (2025) 754–764, https://doi.org/10.1021/accountsmr.5c00053.
[54] F. Hausen, N. Balke, Current understanding of electrochemical strain microscopy to visualize ion behavior on the nanoscale, Curr. Opin. Electrochem. 47 (2024) 101562, https://doi.org/10.1016/j.coelec.2024.101562.
[55] T.F. Otero, H. Grande, J. Rodríguez, A new model for electrochemical oxidation of polypyrrole under conformational relaxation control, J. Electroanal. Chem. 394 (1995) 211–216, https://doi.org/10.1016/0022-0728(95)04033-K.
[56] T.F. Otero, I. Boyano, Comparative study of conducting polymers by the ESCR model, J. Phys. Chem. B 107 (2003) 6730–6738, https://doi.org/10.1021/jp027748j.
[57] S. Zokaei, D. Kim, E. Järsvall, A.M. Fenton, A.R. Weisen, S. Hultmark, P.H. Nguyen, A.M. Matheson, A. Lund, R. Kroon, M.L. Chabinyc, E.D. Gomez, I. Zozoulenko, C. Müller, Tuning of the elastic modulus of a soft polythiophene through molecular doping, Mater. Horiz. 9 (2022) 433–443, https://doi.org/10.1039/d1mh01079d.
[58] L.G. Kaake, B. Gompf, S. Ludwigs, Electrochemical and solvent-driven swelling in a conducting polymer film, Chem. Mater. 35 (2023) 4532–4540, https://doi.org/10.1021/acs.chemmater.3c00849.
[59] C. Dingler, R. Walter, B. Gompf, S. Ludwigs, Situ monitoring of optical constants, conductivity, and swelling of PEDOT:PSS from doped to the fully neutral State, Macromolecules 55 (2022) 1600–1608, https://doi.org/10.1021/acs.macromol.1c02515.
[60] T. Schoetz, C. Ponce de Leon, A. Bund, M. Ueda, Electro-polymerisation and characterisation of PEDOT in lewis basic, neutral and acidic EMImCl-AlCl3 ionic liquid, Electrochim. Acta 263 (2018) 176–183, https://doi.org/10.1016/j.electacta.2018.01.033.